High Temperature Materials and Processes, Vol. 7, Nos. 2 & 3, 1986, 91-100

Thermodynamics and Kinetics of Metallic Alloy Formation by Picosecond Pulsed Laser Irradiation*

F. Spaepen

Division of Applied Sciences, Harvard University, Cambridge, MA 02138, USA

CONTENTS

	Page
1. INTRODUCTION	92
2. PICOSECOND LASER QUENCHING MECHANISM	92
3. THERMODYNAMICS AND KINETICS	94
4. EXPERIMENTAL ASPECTS	96
5. SURVEY OF RESULTS	97
5.1. Fe-B	97
5.2. Ni-Nb	98
5.3. Mo-Ni	98
5.4. Mo-Co	99
5.5. Nb-Co	99
5.6. Ag-Cu	99
5.7. Cu-Co	99
5.8. Nb-Si	99
6. ACKNOWLEDGEMENTS	99
7. REFERENCES	99

* Reprinted from the Nato volume entitled "Laser Surface Treatment," Draper C.W. and Mazzoldi, P. (Eds.) published by Martinus Nijhoff, 1986, with kind permission of the publisher.

ISSN 0334-1704

1. INTRODUCTION

Irradiating a metallic surface with a short laser pulse is a method for confining the deposition of thermal energy to a very thin surface layer, which melts and is subsequently quenched at a very high rate. This makes picosecond pulsed laser quenching the fastest melt quenching method available.

In the first part of the paper, the mechanism of heating and quenching in picosecond laser quenching is analyzed in some detail, and simple estimates are made of the basic quantities (cooling rate, melt lifetime, etc.). The possible effects of evaporation are also discussed, and shown to be negligible in this regime.

The second part of the paper deals with the thermodynamic restrictions on the type of transformations that can occur on the very short timescale of the laser quenching process. Which of these allowed transformations actually occurs is determined by the kinetics of the competing solidification processes. Depending on the degree of the structural rearrangement required to form a crystal from the melt, its growth can be collision- or diffusion-controlled. It will be shown that only the simplest crystal structures or dilute solutions exhibit collision-limited growth, which is fast enough not to be suppressed even by picosecond pulsed laser quenching.

In the last part of the paper, a brief review of the work at Harvard on alloy formation is given. The Fe-B system has been investigated most thoroughly, and phase formation (glass vs. crystal) in this system will be analyzed in some detail. Other alloy systems include: Ni-Nb, Mo-Ni, Co-Mo, Co-Nb, Cu-Ag, Cu-Co, and Nb-Si.

2. PICOSECOND LASER QUENCHING MECHANISM

The process of energy deposition, heating and cooling in pulsed laser irradiation of solid surfaces has been analyzed in detail by a number of authors /1, 2/. Figure 1 illustrates the three stages of the process, using parameters corresponding to the experiments described later.

In the first stage, which lasts for the duration of the pulse, the laser energy is deposited in a layer of thickness α^{-1} (α: absorption coefficient). For optical light metals, α^{-1} is on the order of a few tens of nanometers. Since the transfer of the energy from the electrons, which interact with the laser light, to the lattice occurs on a timescale of less than 1 ps, the process can be described as a thermal one /3/. Over the duration of the pulse, t_p, the thermal diffusion length is $\ell_T = (2D_{th}\, t_p)^{1/2}$. In metals, ℓ_T lies between 25 and 70 nm, depending on the thermal diffusivity ($D_{th} = 10^{-4}$ to 10^{-5} $m^2\, s^{-1}$). Deposition of the absorbed laser energy as heat in a layer of thickness ℓ_T results in its melting and overheating to several thousand degrees.

It is worth noting that for pulse durations of less than 1 ps, ℓ_T becomes less than α^{-1}. In this regime, the thickness of the initial molten layer and the thermal gradients become independent of the pulse length. For this reason, femtosecond pulses, which are very useful for time-resolved

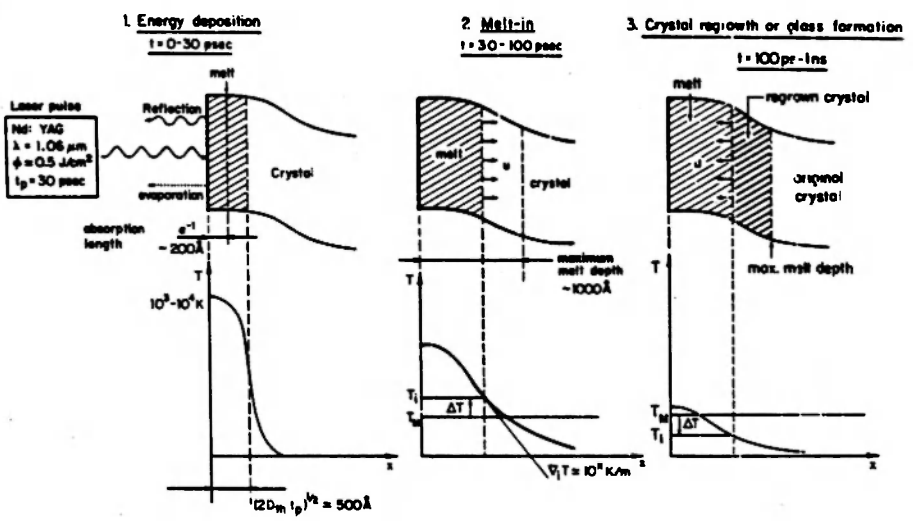

Fig. 1: Schematic illustration of the mechanism of pulsed laser quenching.

probing of the irradiation process, do not produce higher quench rates than picosecond pulses. A general discussion of the ℓ_T vs. α^{-1} regimes is given by Bloembergen /1/.

In the second stage, which starts at the end of the pulse, more of the underlying crystal is melted, until the overheat of the melt is spent. The crystal-melt interface moves away from the surface until its temperature drops to the equilibrium melting temperature. The maximum melt depth, d, for the conditions of Figure 1 (fluence ~ 0.5 J cm^{-2}, reflectivity ~ 0.1) is about 100 nm. Since the thermal gradients in this process are very high (10^{11} K m^{-1}), the melt-in velocity is also large ($u \sim 10^3$ m s^{-1}). The melt-in phase is therefore expected to last only $d/u \sim 100$ ps.

In the third stage, the interface temperature falls below the equilibrium melting temperature, and the crystal-melt interface reverses direction. If the crystal regrowth process is fast enough, the entire melt is consumed. Otherwise, i.e., if the melt cools to its configurational freezing point before crystallizing, a glass is formed. The thermal parameters in this regrowth process have been analyzed by sophisticated numerical methods (especially for silicon), but their order of magnitude can easily be estimated from dimensional arguments. The temperature scale is determined by the melting temperature, T_m, which is on the order of 10^3 K. The length scale is set by the melt depth $d \sim 10^{-7}$ m. The average thermal gradient is then $\nabla T = T_m/d \sim 10^{10}$ K m^{-1}, and the corresponding cooling rate is $\dot{T} = D_{th} T/d \sim 10^{12}$ K s^{-1}. The lifetime of the melt, τ, is an important experimental parameter, which can be estimated as $\tau = T_m/\dot{T} = 10^{-9}$ s. This estimate is in agreement with transient reflectivity measurements, which show τ to be on the order of a few nanoseconds /4-6/. In the analysis of crystal growth rate vs. heat removal, it is useful to know the velocity, u_T, with which isotherms move toward the surface during cooling. A simple linear estimate gives: $u_T = \dot{T}/\nabla T \sim 100$ m s^{-1}.

These parameters are summarized in Table 1. For comparison, the parameters for conventional melt spinning are also listed. The main difference there is the greater thickness of the melt, which brings the cooling rate, $\dot{T} \sim d^{-2}$, down to 10^6 K s^{-1}.

The rate of evaporation during laser quenching can be estimated from the kinetic theory of gases. The number of atoms leaving a unit surface per second, which is, in equilibrium, equal to the number arriving from the vapor at a pressure p, is given by $\Gamma = p/(2\pi k_B T M)^{1/2}$ (k_B: Boltzmann's constant; M: atomic mass). At the boiling point, T_b, p = 1 atm, and $\Gamma = 10^{-23}$ cm^{-2} s^{-1}, or 10^8 monolayers per second. Over the lifetime of the melt this corresponds to a loss of less than a monolayer. During the energy deposition stage, the surface temperature can briefly rise to several thousand degrees above T_b, and the corresponding equilibrium vapor pressure of 10^4 atm. The duration of this extreme overheat is very short, however ($< t_p = 30$ ps), so that the evaporation loss is at most a few tens of monolayers. The energy loss rate due to evaporation is $\Gamma \Delta h_v/N$ (Δh_v: molar heat of evaporation, $\sim 10^5$ J mole^{-1}, N: Avogadro's number), which is at most 10^8 W cm^{-2}. This is still considerably below the absorbed laser intensity of 10^9 W cm^{-2}, and hence negligible as an energy loss.

TABLE 1. Thermal Parameters in Melt Quenching (from ref. /2/)

		Laser quenching	Melt spinning
Melt temperature	T_m (K)	10^3	10^3
Melt thickness	d (m)	10^{-7}	5×10^{-5}
Temperature gradient	∇T (K/m)	10^{10}	2×10^7
Cooling rate	$\dot{T}$ (K/s)	10^{12}	4×10^6
Melt lifetime	τ (s)	10^{-9}	not applicable
Isotherm velocity	u_T (m/s)	100	0.2
Heat-flow limited crystal growth velocity	u_h (m/s)	230	0.5

The accuracy of these estimates was checked in a simple experiment /7, 8/. A thin metallic ribbon was clamped at one end and irradiated with the laser pulse at the other end. The recoil pressure of the evaporation (equal to half the vapor pressure) makes the ribbon oscillate visibly. By measuring the amplitude of the oscillation and the bending stiffness of the ribbon, the recoil pressure could be determined. A value of 10^{10} N m^{-2} was found, which is indeed similar to the peak vapor pressure estimated above.

The holes often found after irradiation of a surface are therefore *not* the result of evaporation *per se*, but of *mechanical* displacement of the liquid by the large recoil pressure of the evaporation ("splashing"). Often the morphology of the displaced material around the hole is direct evidence of splashing. Also, in some experiments on thin

films supported on a different substrate, substrate atoms are sometimes detected on the top surface of the film in the vicinity of the hole; this, too, can only be explained by splashing.

3. THERMODYNAMICS AND KINETICS

The short timescale of the picosecond melt quenching process puts restrictions on the type of transformations that can occur. For the entire molten layer to be crystallized in the regrowth stage of Figure 3, the crystal-melt interface velocity must be on the order of $u = d/\tau \sim 100\ m\ s^{-1}$. Note that this is also the isotherm velocity, u_T, of Table 1. If the interface lags behind the isotherms, crystal growth may be preempted by glass formation. The time required to crystallize the monolayer of thickness $\lambda = 0.3$ nm at a growth speed u is $t_1 = \lambda/u \sim 3$ ps. The distance an atom can diffuse in this amount of time, $(D_\ell t_1)^{1/2}$, is less than an interatomic distance (D:liquid diffusivity: 10^{-8} to $10^{-9}\ m^2\ s^{-1}$). This means that no long-range atomic transport can occur under these conditions, and that the only type of transformation that can occur is *partitionless* solidification, either by growth of a crystal of the same composition as the melt or by formation of a glass.

The thermodynamic conditions for partitionless crystallization are illustrated on the phase diagram of Figure 2, which contains two primary solid solutions (α, δ) and two intermetallic compounds (β, γ). The free energy diagram at temperature T_1 shows that partitionless crystallization of the liquid (ℓ) to the primary solution δ can only occur for compositions x greater than $x_{0,\delta\ell}$, at the intersection of the free energy curves. The locus of the points $x_{0,\delta\ell}$ for all temperatures forms the $T_{0\,\delta\ell}$-line. Partitionless crystallization to the δ-phase can only occur below this T_0-line. For the other phases, similar T_0-lines are shown. At a sufficiently low temperature, T_g, the atomic transport rate (diffusivity) in the liquid state becomes negligibly small, so that no transformations can occur on a reasonable timescale. The liquid is then configurationally frozen and becomes a glass. For a composition in the range x' – x" in Figure 2, no crystallization is possible under picosecond laser quenching conditions, and therefore only glass formation is thermodynamically possible. This thermodynamic criterion for glass formation, however, is only a *sufficient* one, and not a necessary one as has been

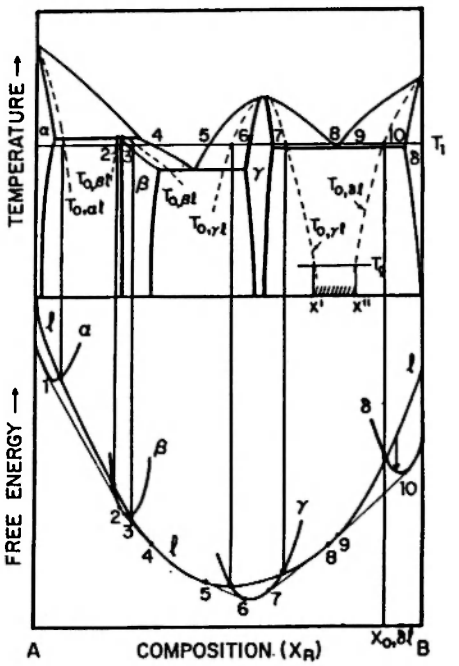

Fig. 2. Schematic phase diagram (top), and corresponding free energy diagram at temperature T_1 (bottom), illustrating the construction of the T_0-lines for the primary solutions and the intermetallic compounds. In the composition range x'–x" (dashed), only glass formation is possible under conditions of partitionless solidification. The numbers correspond to the same compositions in the top and bottom diagrams.

claimed by some authors /9, 10/. To formulate the glass-forming criterion more strictly, it is necessary to consider also the kinetics of partitionless crystallization.

As discussed in a number of previous papers /11, 12/, the crystal growth velocity, u, can be written as:

$$u = fk\lambda\,[1 - \exp(-\frac{\Delta G_c}{RT_i})] \qquad (1)$$

where:

- k: atom jump frequency across the crystal-melt interface;
- f: fraction of interface sites that can incorporate a new atom;
- ΔG_c: difference in molar free energy between crystal and melt (driving free energy, taken positive for undercooling);
- T_i: interface temperature.

If T_i is not too far below T_m, so that the difference in molar entropy between crystal and melt,

ΔS_c, can be considered constant with temperature, the driving free energy can be written as:

$$\Delta G_c = \Delta S_c(T_m - T_i) \quad (2)$$

For small ΔG_c, the exponential in equation (1) can be expanded and linearized:

$$u = fk\lambda \frac{\Delta G_c}{RT_i} \quad (3)$$

or, with equation (2):

$$u = fk\lambda \frac{\Delta S_c}{R} \frac{T_m - T_i}{T_i} \quad (4)$$

where, for metals, $f \doteq 1$ and $S_c \doteq R$.

The crystal growth rate is also determined by the rate at which the latent heat of crystallization, ΔH_c per mole, can be removed. The heat flux corresponding to a velocity u is:

$$\dot{Q} = \frac{u\Delta H_c}{\bar{V}} \quad (5)$$

where $\bar{V}$ is the molar volume.

Since this heat must be removed through conduction down the temperature gradient at the interface, $\nabla_i T$, this flux is also:

$$\dot{Q} = \kappa \nabla_i T \quad (6)$$

where the κ is the thermal conductivity.

Combining equations (5) and (6) allows definition of a heat flow limited velocity:

$$u_h = \frac{k\bar{V}\nabla_i T}{\Delta H_c} \quad (7)$$

Table 1 lists typical values of u_h for Fe, under both laser quenching and melt spinning conditions, using the tabulated value of the temperature gradient for $\nabla_i T$. That u_h and u_T have similar values is a direct result of ΔS_c and the molar specific heat, C, being of the same order of magnitude.

Since the crystal growth velocity in equations (4) and (7) must be the same, they can be combined for metals as:

$$\frac{u_h}{k\lambda} = \frac{T_m - T_i}{T_i} \quad (8)$$

In conventional solidification, the interface kinetics are much faster than the rate of heat removal, so that: $u_{th} \ll k\lambda$, and T_i is close to T_m. The growth is said to be *heat flow-limited.* In laser quenching, depending on the nature of the interface rearrangements (to be discussed below), the rate of heat removal, due to the very steep gradient, can be much faster than the crystal growth kinetics, so that $u_{th} \gg k\lambda$, and $T_i \ll T_m$. The growth is said to be *interface-limited.* At such large undercoolings, metastable phases and glasses can be formed.

The value of $k\lambda$ is determined by the nature of the atomic rearrangements necessary to advance the crystal-melt interface. In pure metals, dilute alloys, or crystalline compounds with a simple structure, k can be taken as the thermal vibration frequency. The maximum growth velocity $u_{max,c} = k\lambda$ can then be taken as the speed of sound, u_s, in the liquid. This is the *collision-controlled* regime, which is treated in more detail in another paper in this chapter /6/. Suffice it to point out here that, even in picosecond laser quenching, under the conditions of Table 1, $u_{max} \ll u_T, u_h$, which makes this type of growth difficult to suppress.

In more concentrated alloys, or compounds with a more complicated crystal structure, which require changes in nearest neighbors upon crystallization, k is a diffusive jump frequency, and can be taken as D/λ^2. The maximum growth velocity in this *diffusion-controlled* regime is $u_{max,D} = D/\lambda$, which is on the order of 10 m/s. Table 1 shows that for picosecond laser quenching, $u_{max,D} \ll u_T, u_h$, so that this type of growth can easily be suppressed. It follows then from equation (8) that T_i must fall far below T_m, and that glass formation becomes possible. It should also be noted here that the temperature dependence of the liquid diffusivity has a Fulcher-Vogel form $D_\ell = D_0 \exp[B/(T - T_0)]$, which makes D_ℓ, and hence k, become negligibly small in the vicinity of T_0 (i.e., around T_g) /13/.

Although the partitionless growth of intermetallic compounds occurs, by definition, without *long-range* diffusional transport, the growth can still be diffusion-controlled if a drastic rearrangement of the nearest neighbor environment is required to transform the liquid structure into the crystalline one. This is the case if the crystalline unit cell is large, or if long-range chemical order must be established. In the example of Figure 2, if the forma-

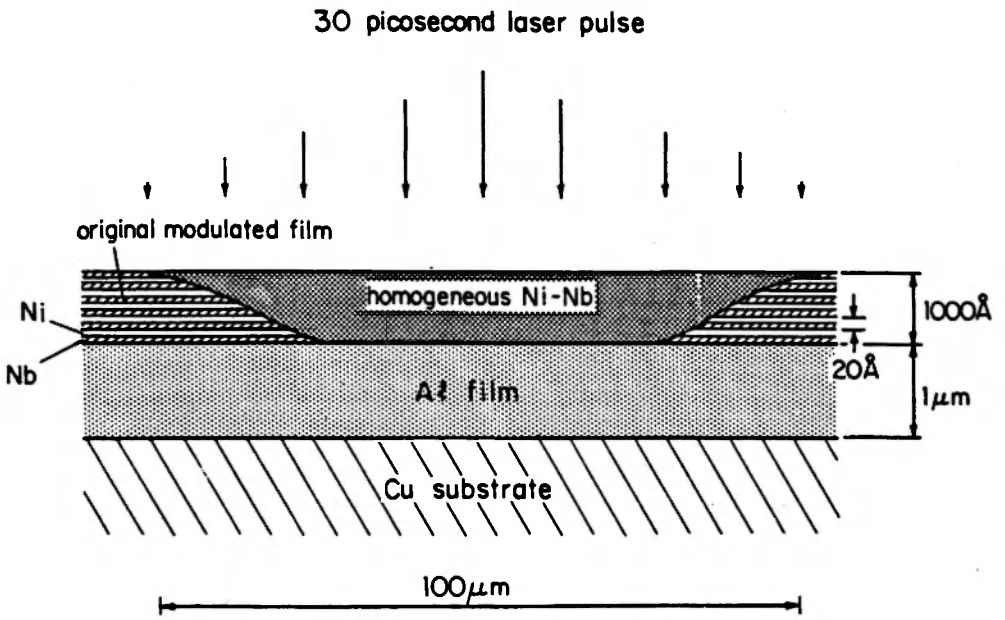

Fig. 3. Schematic diagram, drawn to a variable scale, of a multilayer film after irradiation with a 30 ps laser pulse with a Gaussian intensity profile. From /25/.

tion of the compounds β and γ is diffusion-controlled, even below their respective T_0-line, their formation is suppressed in picosecond laser quenching and the intersections of the $T_{0,\alpha\ell}$ and $T_{0,\delta\ell}$ lines with the T_g-line can be used to define a new glass formation range.

This criterion, however, can still be extended, since in many systems glasses can be formed far below the T_0-lines of the primary solid solutions. Several examples will be discussed below. Again, partitionless formation of the primary solid solutions can be diffusion-controlled, and hence suppressed by picosecond pulsed laser quenching, if the change in short-range order between liquid and crystal is considerable.

4. EXPERIMENTAL ASPECTS

The short lifetime of the melt (τ = 1 ns) creates a special problem in obtaining a homogeneous melt, which is necessary for systematic studies of phase formation. The mixing length in the liquid, $(D_\ell\tau)^{1/2}$, is only 3 nm. The alloy components must therefore be mixed on this scale in the starting sample. This can be accomplished in a number of ways, such as ion implantation, co-evaporation, or deposition of multilayers. The latter method is a particularly convenient one that has been used for all the experiments discussed below. A typical sample geometry is drawn in Figure 3. The Al film is evaporated onto the Cu substrate. The multilayer is produced by alternate sputter deposition of the elemental metals, or a metal and an alloy, from two targets /14, 16/. The average film composition can be varied conveniently by changing the thickness ratio of the layers. By keeping the repeat length of the multilayers below 3 nm, homogenization is achieved upon melting. This was checked experimentally on a Cu-Ag alloy from a Cu/Ag multilayer /7, 8/. As expected, a metastable fcc solid solution was formed, which had a *single* lattice parameter, corresponding to the average composition of the film. No evidence of quenched-in homogeneity was found.

After irradiation, the samples can easily be removed from the substrate by dissolving the Al in NaOH. Note that Al is also a good material for a heat sink. Since the films are only 100 nm thick ($\sim$ melt depth), they can be investigated by electron microscopy without further thinning.

The reproducibility of the laser system used in the experiments discussed below was insufficient to pre-set the fluence levels predictably. Therefore, on each sample, a series of irradiations were made at different fluence levels. Subsequent investigation was then done on those spots that had a small hole (a few μm) at their center, due to "splashing" in-

duced by the most intense part of the Gaussian beam. These spots were known to have received a fluence large enough to induce melting, and still had a large amount of material available for study.

5. SURVEY OF RESULTS

5.1. Fe-B

This system has been studied in the 12–28 at.% B range /2, 17-19/. The starting samples consisted of multi-layered α-Fe and amorphous Fe_3B. It was found that alloys containing a minimum of 5 at.% B were amorphous after picosecond laser quenching. Below 5 at.% B, the solidification product was a Fe(B) bcc interstitial solution. The 4 at.% alloy showed a small amount of amorphous material near the top surface of the film /19/; it was distributed in a morphology characteristic of an interfacial instability, which could have become possible at the last stage of the solidification when the crystal growth velocity decreases considerably /20/. The redistribution of the B associated with the instability could then have led to glass formation in the B-rich regions.

The T_0-line for the ℓ → bcc transformation can be calculated fairly accurately from the phase diagram using simple regular solution theory /2, 8/. The result is shown in Figure 4, and is in agreement with the observation that Fe-B glasses with less than 18 at.% B crystallize into the bcc Fe(B) solution upon heating /21/. The crystallization temperature for an 18 at.% B glass is 660 K, which corresponds to 16 at.% B on the T_0-line.

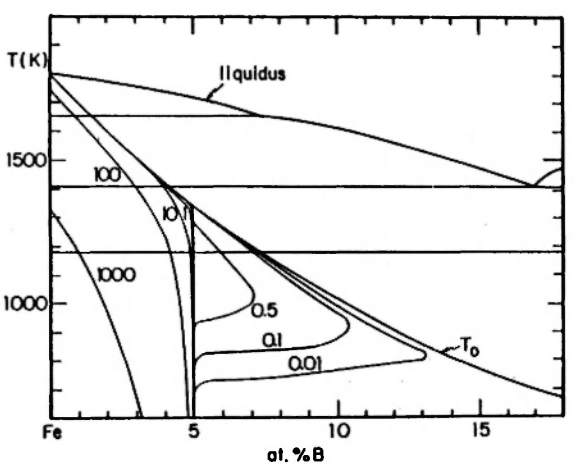

Fig. 4: The Fe-B phase diagram, showing the T_0 line for the liquid → bcc transition. The contours represent the bcc crystal growth speed (in m s^{-1}) as a function of composition and interface temperature, calculated from the model explained in the text. From (2).

The Fe-B glasses clearly form far below the T_0-line ($T_0 - T_g$ is 700 K for a 5 at.% B alloy). As explained above, the growth of the competing bcc phase must therefore be diffusion-controlled in alloys with more than 5 at.% B. Given that the nearest neighbor environment of a B-atom in a Fe-B glass consists of nine Fe atoms in a trigonal prismatic arrangement /22/, which is very different from the nearest neighbor environment of an interstitial B in the bcc Fe(B) solution, this diffusional control is to be expected. The glass-forming limit of 5 at.% B suggests that each B atom forms a cluster of about 19 Fe atoms (i.e., one and one-half coordination shells) around it that must be rearranged upon crystallization. The rest of the Fe atoms behave as in pure Fe, and make collisional jumps. The maximum velocity in equation (1) can then be written as (2):

$$f k \lambda = (20 x_B) \frac{D_\ell}{\lambda} + (1 - 20 x_B) u_s \quad \text{for } x_B \leqslant 0.05$$

$$= D_\ell / \lambda \quad \text{for } x_B > 0.05 \qquad (9)$$

where x_B is the atom fraction of B.

Using a temperature dependence for the diffusivity:

$$D_\ell = 1.4 \times 10^{-8} \exp\left[- \frac{1300}{T - 581} \right] m^2 s^{-1} \qquad (10)$$

obtained by fitting liquid and glass transport data, and a driving free energy:

$$\Delta G_c = (x_{Fe} \Delta S_{c,Fe} + x_B \Delta S_{c,B})(T - T_0) \qquad (11)$$

with $\Delta S_{c,Fe} = 7.6$ J K. ^{1} $mole^{-1}$ and $\Delta S_{c,B} = 21.8$ J K^{-1} $mole^{-1}$, the crystal growth velocity could be calculated as a function of composition and temperature. The results are shown in Figures 4 and 5. Note that crystallization is driven by the undercooling below T_0, not below the liquids temperature. Figure 5 shows clearly that the isotherm

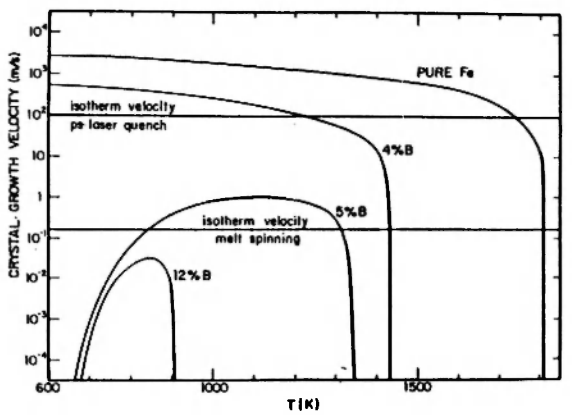

Fig. 5: Growth velocity of the bcc crystal as a function of interface temperature for four composition in the Fe-B system. From (2).

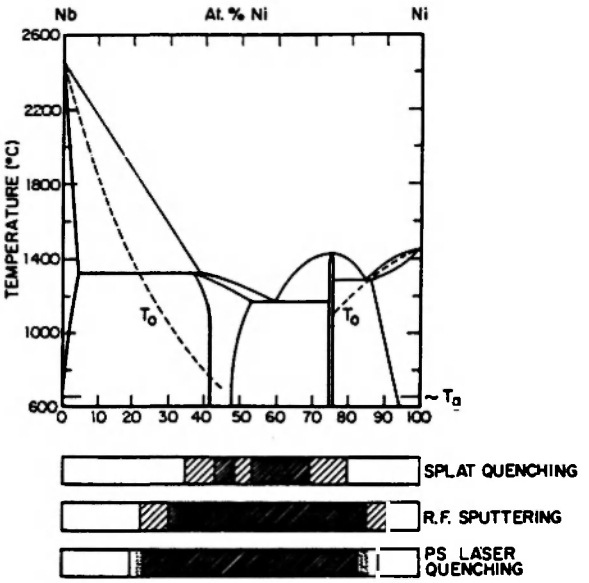

Fig. 6: Equilibrium phase diagram for the Ni-Nb system, with calculated T_0-lines. T_g indicates the approximate crystallization temperature of nearly equiatomic amorphous alloys (34). The glass-forming ranges for splat quenching (28), RF sputtering (29) and picosecond laser quenching (25) are indicated. Fine hatching: fully amorphous; coarse hatching: mixed amorphous and crystalline; dashed hatching indicates that the glass formation limits for picosecond laser quenching are between the surrounding vertical lines. From (25).

velocity in picosecond laser quenching is large enough to prevent crystal growth in a 5 at.% B alloy, but not in a 4 at.% alloy. It is interesting that the simple estimates of Table 1 can also account for the minimum of 12 at.% B necessary in melt spinning to obtain a glass /21, 23, 24/.

5.2. *Ni-Nb*

This system has been studied over the entire composition range /25/. The starting materials were multilayers of the elemental metals. As illustrated on Figure 6, a glass was obtained by picosecond laser quenching in the range 23–82 at.% Ni. This range exceeds that for splat quenching /26/ ($\sim 10^{10}$ K s^{-1} /27, 28/)and for RF sputtering of homogeneous films /29/. It is interesting that the cooling rate in the latter process is estimated at about 10^{13} K s^{-1} /30/, similar to that for laser quenching. None of the intermetallic compounds, the μ-phase or the Ni_3Nb phase, were formed even if the melt composition was close. This indicates that their growth is diffusion-controlled, which is to be expected for the size of their unit cell and degree of order.

The T_0-lines for the primary solutions on Figure 6 have been calculated from the phase diagram using simple regular solution theory. In this system also, glasses are formed far below the T_0-line ($T_g \sim 940$ K /34/). A mechanism similar to that discussed for Fe-B probably also makes growth of these supersaturated primary solutions diffusion-controlled. That the minimum amount of solute required for glass formation is greater here than for Fe-B may reflect the lesser interaction, and hence smaller cluster size, in metal-metal alloys than in metal-metalloid alloys.

Below 18 at.% Ni supersaturated bcc solutions were formed. Above 89 at.% Ni supersaturated fcc solutions, containing many twins and stacking faults, were formed. The defect density increased with Nb content, probably due to a lowering of the stacking fault energy. Growth twins are also formed in the regrowth of silicon (fcc) from the melt following a laser pulse, at growth velocities intermediate between those of the perfect crystal and the amorphous phase /31/.

5.3. *Mo-Ni*

Glasses were formed, for the first time by melt quenching, in alloys with 30, 50 and 60 at.% Ni /32/. The 50 at.% Ni alloy corresponds to an intermetallic compound in equilibrium (δ-phase). Due to its large unit cell (56 atoms Frank-Kasper phase), it is not formed in picosecond laser quenching. The other two glasses again formed far below the T_0-line.

5.4. Mo-Co

A 45 at.% Co alloy was quenched to a glass for the first time by this method /32/. The ϵ-phase, at the same composition, is not formed.

5.5. Nb-Co

A glass was formed at 40 at.% Nb /32/. The γ-phase is not formed, even though glass formation probably occurred below the $T_{0,\gamma\ell}$ line.

5.6. Ag-Cu

A disordered fcc phase was formed upon quenching of 35, 50 and 65 at.% Ag alloys /7/. This is to be expected, since the crystallization kinetics of a disordered fcc crystal are no different from those of a pure fcc crystal, which are known to be collision-controlled, and hence difficult to suppress. Note that the T_0-line reaches across the phase diagram of Figure 7, so that crystallization of the fcc phase is the dominating process at all compositions.

5.7. Cu-Co

A disordered fcc phase was formed at 50 at.% Co /7/. Again, the T_0-line for this phase spans the phase diagram.

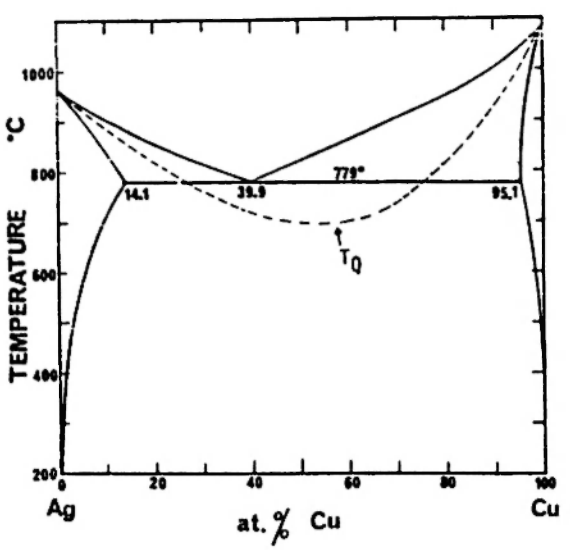

Fig. 7: Ag-Cu equilibrium phase diagram. The T_0-line has been calculated using the regular solution model. From (8).

5.8. Nb-Si

A fcc phase was formed in the composition range 10–27 at.% Si /33/. So far, this phase had only been prepared at 22 at.% Si by shock compression.

6. ACKNOWLEDGEMENTS

The work described in this paper has been performed in collaboration with C.J. Lin and W.K. Wang. It is supported by the Office of Naval Research under Contract No. N00014-83-K-0030.

7. REFERENCES

1. BLOEMBERGEN, N., in "Laser-Solid Interactions and Laser Processing", edited by S.D. Ferris, H.J. Leamy and J.M. Poate, p. 1, AIP, New York (1979).
2. SPAEPEN, F. and LIN, C.J., in "Amorphous Metals and Non-Equilibrium Processing", edited by M. von Allmen, p. 65, Les Editions de Physique, Les Ulis, France (1984).
3. For a review of these relaxation processes, see BROWN, W.L., *Mater. Res. Soc. Symp. Proc.*, **23**: 9 (1984).
4. LIU, J.M., YEN, R., KURZ, H. and BLOEMBERGEN, N., *Appl. Phys. Lett.*, **39**: 755 (1981).
5. BUCKSBAUM, P.H. and BOKOR, J., *Mater. Res. Soc. Symp. Proc.*, **13**: 51 (1983).
6. MACDONALD, C.A. and SPAEPEN, F., in NATO-ASI Proc., edited by C.W. Draper and P. Mazzoldi, Kluwer Publishers, Hingham, Mass. (1986).
7. LIN, C.J. and SPAEPEN, F., *Mater. Res. Soc. Symp. Proc.*, **28**: 75 (1984).
8. LIN, C.J., Ph.D. Thesis, Harvard University (1983).
9. MASSALSKI, T.B., Proc. 4th Int. Conf. on Rapidly Quenched Metals, edited by T. Masumoto and K. Suzuki, p. 203, Jpn. Inst. Metals, Sendai (1982).
10. BOETTINGER, W.J., *ibid.* p. 99.
11. TURNBULL, D., in "Physical Processes in Laser-Materials Interactions", NATO-ASI Proc., edited by M. Bertollotti, p. 117, Plenum, New York (1983).
12. SPAEPEN, F. and TURNBULL, D., in "Laser Processing of Semiconductors", edited by J.M. Poate and J.W. Mayer, p. 15, Academic, New York (1982).
13. For a review of atomic transport in liquids and glasses, see SPAEPEN, F. and TAUB, A.I., in "Amorphous Metallic Alloys", edited by F.E. Luborsky, p. 231, Butterworths, London (1983); CANTOR, B. and CAHN, R.W., *ibid.*, p. 487.
14. ROSENBLUM, M.P., SPAEPEN, F. and TURNBULL, D., *Appl. Phys. Lett.*, **37**: 184 (1982).
15. GREER, A.L., LIN, C.J. and SPAEPEN, F., Proc. 4th Int. Conf. on Rapidly Quenched Metals, edited

by T. Masumoto and K. Suzuki, p. 567, Jpn. Inst. Metals, Sendai (1982).
16. SPAEPEN, F., GREER, A.L., KELTON, K.F. and BELL, J.L., *Rev. Sci. Instrum.*, **56**: 1340 (1985).
17. LIN, C.J. and SPAEPEN, F., *Appl. Phys. Lett.*, **41**: 721 (1982).
18. LIN, C.J. and SPAEPEN, F., in "Chemistry of Physics of Rapidly Solidified Materials", edited by B.J. Berkowitz and R.O. Scattergood, p. 273, TMS-AIME, New York (1983).
19. LIN, C.J. and SPAEPEN, F., *Scr. Metall.*, **17**: 1259 (1983).
20. CAHN, J.W., CORIELL, S.R. and BOETTINGER, W.J., in "Laser and Electron Beam Processing of Materials", edited by C.W. White and P.S. Peercy, p. 89, Academic, New York (1980).
21. HASEGAWA, R. and RAY, R., *J. Appl. Phys.*, **49**: 4174 (1978).
22. For a review of the short-range order in metal-metalloid glasses, see DUBOIS, J.M. and LECAER, G., *Acta Metall.*, **32**: 2101 (1984).
23. RAY, R. and HASEGAWA, R., *Solid State Commun.*, **27**: 471 (1978).
24. LUBORSKY, F.E. and LIEBERMANN, H.H., *Appl. Phys. Lett.*, **33**: 233 (1978).
25. LIN, C.J. and SPAEPEN, F., *Acta Metall.*, **34**: 1367 (1986).
26. RUHL, R.C., GIESSEN, B.C., COHEN, M. and GRANT, N.J., *Acta Metall.*, **15**: 1693 (1967).
27. DUWEZ, P. and WILLENS, R.H., *Trans. Met. Soc. AIME*, **227**: 362 (1963).
28. JONES, H., Proc. 2nd Int. Conf. on Rapidly Quenched Metals, edited by B.C. Giessen and N.J. Grant, p. 1, MIT Press, Cambridge, MA (1976).
29. BARBEE, T.W., HOLMES, W.H., KEITH, D.L., PYZYNA, M.K. and ILONCA, G., *Thin Solid Films*, **45**: 591 (1977).
30. TURNBULL, D., *Metall. Trans.*, **A12**: 695 (1981).
31. CULLIS, A.G., CHEW, N.G., WEBBER, H.C. and SMITH, D.J., *J. Cryst. Growth*, **68**: 624 (1984).
32. LIN, C.J., SPAEPEN, F. and TURNBULL, D., *J. Non-Cryst. Solids*, **61/62**: 767 (1984).
33. WANG, W.K. and SPAEPEN, F., *J. Appl. Phys.*, **58**: 4477 (1985).
34. GIESSEN, B.C., MADHAVA, M., POLK, D.E. and VANDER SANDE, J., *Mater. Sci. Eng.*, **23**: 145 (1976).